Modeling and Simulation of 3D EMF Processes[1]

J. Unger[1], M. Stiemer[2], M. Schwarze[3], B. Svendsen[1], H. Blum[2], S. Reese[3]

[1]Chair of Scientific Computing, TU Dortmund
[2]Chair of Mechanics, TU Dortmund
[3]Institute of Solid Mechanics, TU Braunschweig

Abstract

A recent interest in potential industrial applications of electromagnetic forming processes has inspired a demand for adequate simulation tools. Aiming at the virtual design of industrial applications, the purpose of this work is to develop algorithmic formulations particularly suitable to reduce the enormous computational cost inherent to 3D simulations. These formulations comprise a carefully chosen discretization, highly accurate methods for data transfer between electromagnetic and mechanical subsystems, an efficient solid shell formulation, and a termination criterion for the electromagnetic field computation. As a result the simulation time is reduced by about one order of magnitude.

Keywords:

Modeling, electromagnetic metal forming

1 Introduction

Electromagnetic forming (EMF) is a dynamic, high strain-rate forming method in which strain-rates of 10^3 s^{-1} arise. The deformation of the work piece is driven by the interaction of a pulsed magnetic field triggered by a nearby tool coil with eddy currents induced in the work piece. This interaction effects a material body force, the Lorentz force, and the electromotive power, representing an additional supply of momentum and energy to the material. On the other hand the electromagnetic part of the system is sensitively influenced by the spatio-temporal evolution of the deformation of the mechanical structure. An increasing interest

[1] *This work was carried out in the context of the German National Science Foundation (Deutsche Forschungsgemeinschaft (DFG)) Research Group FOR 443. The authors wish to thank the DFG for its financial support.*

in this forming operation, recently caused a considerable effort to simulate such coupled processes. However, approaches reported on so far were mainly restricted to axisymmetric geometries [1, 2, 3, 4, 5] or to small deformation problems [6]. Yet, it is the 3D modeling capability in combination with the large inelastic deformations that is required to advance effectively in the design of industrial EMF processes. To meet these modeling requirements the sound derivation of a physical model of the relevant magneto-mechanical phenomena has been presented in [7]. It is algorithmically implemented in [8] and [9].

While typical 2D models of EMF in general exhibit a size of between about 3000 and 10000 degrees of freedom, the number of degrees of freedom for similar 3D models is about one order of magnitude higher. Consequently, the requirements of a three dimensional simulation often exceed the computational resources contemporary computers offer. The goal of the present work is to develop new approaches to the simulation of relevant 3D models for EMF that reduce the computational cost to a range that allows for numerical simulations on contemporary computers. A main result is an accurate and efficient coupling scheme of the electromagnetic and mechanical subsystems that enables the use of solid shell elements [10] (Section 2). Further, a termination criterion for the electromagnetic part of the model leads to a significant gain in efficiency (Section 3). In Section 4 the benefit of all these methods is validated with a fully coupled forming operation. All developed methods will be demonstraded by means of a particular model problem. Although the presented forming geometry is rather exceptional (see Figure 1), dimensions and timescales carry over to other geometries. The coupled multifield model for electromagnetic forming considered here represents a special case of the general continuum thermodynamic formulation for inelastic non-polarizable and non-magnetizable materials given in [7]. In summary, this special case is based on the quasi-static approximation to Maxwell's equations, in which the wave character of the electromagnetic fields is neglected. In this case, the unknown fields of interest are the motion field $\boldsymbol{\xi}$, the scalar potential χ and the vector potential $\boldsymbol{a}$ determining in particular the magnetic field in the usual fashion [11]. Assuming Dirichlet boundary conditions for all fields, one derives the weak field relations

$$
\begin{aligned}
0 &= \int_{B_r} (\varrho_r \ddot{\boldsymbol{\xi}} - \boldsymbol{l}_r) \cdot \boldsymbol{\xi}_* + \boldsymbol{K}\boldsymbol{F}^{-\mathsf{T}} \cdot \nabla \boldsymbol{\xi}_* \,, \\
0 &= \int_R \{\dot{\boldsymbol{a}} + \boldsymbol{L}^{\mathsf{T}} \boldsymbol{a}\} \cdot \boldsymbol{a}_* + \int_R (\chi - \boldsymbol{a} \cdot \boldsymbol{v}) \operatorname{div} \boldsymbol{a}_* + \kappa_{\mathsf{EM}} \operatorname{curl} \boldsymbol{a} \cdot \operatorname{curl} \boldsymbol{a}_* \,, \\
0 &= \int_R \nabla \chi \cdot \nabla \chi_* \,,
\end{aligned}
\tag{1}
$$

for $\boldsymbol{\xi}$, $\boldsymbol{a}$, and χ, respectively. Here, $\boldsymbol{\xi}_*$, $\boldsymbol{a}_*$, and χ_* represent the corresponding test fields. Further, R represents a fixed region in Euclidean point space containing the system under consideration in which the electromagnetic fields exist and on whose boundary the boundary conditions for these fields are specified. Here, the system comprises the sheet metal consisting of the aluminum alloy AA 6060, the tool coil consisting of technically pure copper and air (see Figure 1). Electromagnetic and mechanical material properties of the system can be found in [8].

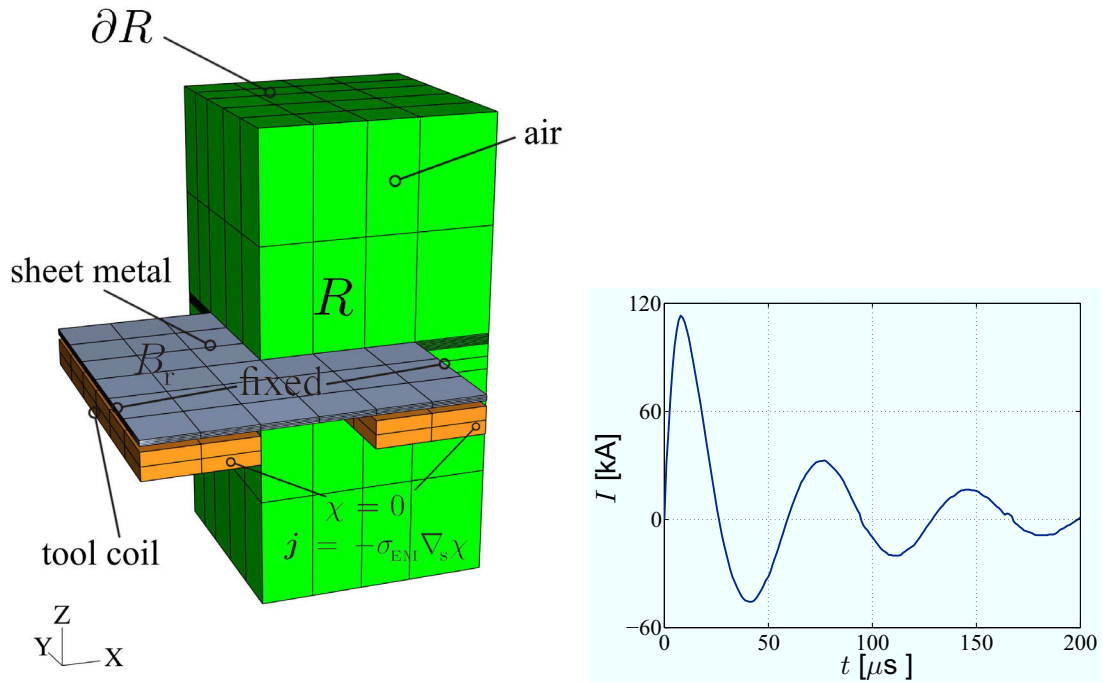

Figure 1: Exemplary forming setup including tool coil, sheet metal, and air. Here, R denotes the whole computational domain with boundary ∂R and B_r the mechanical domain. At ∂R homogeneous Dirichlet boundary conditions are assumed. The experimentally measured input current is implemented as a Neumann boundary condition for the electric scalar potential. On the mechanical side, the lateral edges of the sheet metal are fixed.

2 Mesh Adaption and Data Transfer for Solid Shell Elements

In the case of a staggered approach the solution of the coupled system is computed on two meshes. In [8] a coupled simulation has been presented where the discretization of the electromagnetic subsystem was based on an Eulerian formulation of the discrete system. This means that the Lagrangian mesh for the mechanical structure is moved over a *fixed* Eulerian mesh for the electromagnetic field. However, there are problems inherent to this approach since a contribution to the mass matrix arises as soon as a point is covered by the structure and it disappears when it is uncovered again (see Figure 2 above right). Methods that rely on this Euler-Lagrange approach are sometimes called fictitious boundary methods It has turned out that this change of the discretization causes oscillations in the time derivative of the vector potential and thus in the Lorentz force. If a good approximation to the forces is required an ALE-based method is more promising. Here, the position of the electromagnetic mesh is adapted to the current position of the structure so that the local discretizations never changes (see Figure 2 below right and left). The ALE-mesh adaption is based on a Lagrangian smoothing algorithm [12]. In the above example deformation and body force data are transferred from each single element to each element. In this respect, both discretizations can not be chosen independently. This situation can lead to an unnecessary refinement of one of the subdomains when it is necessary to refine the other

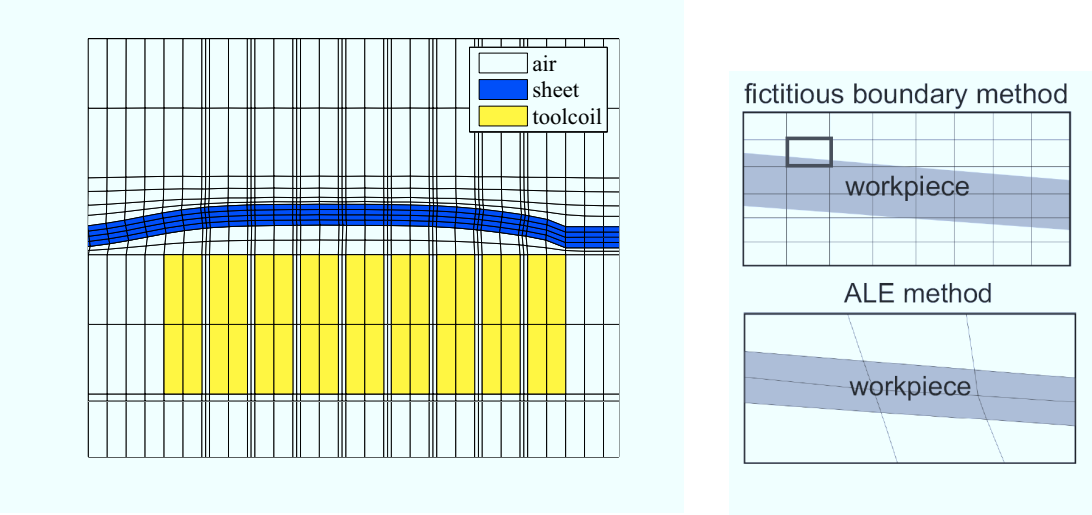

Figure 2: Interaction between the mechanical and electromagnetic mesh. Left: 2D Modeling of an EMF process by means of the ALE algorithm. Right: Schematics of the fictitious boundary method (fixed Eulerian mesh) and the ALE method (matching meshes).

(see mesh in Figure 2 left). Considering the complexity of 3D EMF simulations, there is a strong motivation to refine both meshes independently. This requirement becomes even more significant if shell elements – commonly used in sheet forming simulations – are used for the mechanical mesh. The discretization in thickness direction of the mechanical mesh is then fixed to one layer of elements, which is by far to wide for accurate electromagnetic field computation under typical situations. Here, an independent mesh refinement in thickness direction of the electromagnetic component of the sheet metal is mandatory.

The approach presented here is based on the fact that at t = 0 the boundaries of the discretized electromagnetic and mechanical domain overlap. Later the sheet deforms and the vertex positions $\tilde{\mathbf{x}}$ of the electromagnetic mesh elements have to be adopted such that mesh domains are congruent again. To achieve this, the vertex positions of the electromagnetic elements of the sheet metal are moved according to the mechanical deformation first and then the remaining vertex positions of the electromagnetic mesh are adapted. In the example shown in Figure 2 on the left, the vertices of the elements in the sheet of both the mechanical and the electromagnetic mesh match. In contrast, this is not the case when solid shell elements are used. A mapping of the mechanical deformation to those vertices of the electromagnetic mesh which are contained in the sheet metal is required. One proximate approach to achieve this is given by the simple shape function mapping of the actual nodal element positions $\mathbf{x}^e(t_n)$

$$\tilde{\mathbf{x}}^i_{\mathrm{SM}}(t_n) = \mathbf{H}(\zeta^i(\tilde{\mathbf{x}}^i_{\mathrm{SM}}(t_n))\mathbf{x}^e(t_n) \tag{2}$$

to the element vertex i contained in the sheet metal yielding its new position $\tilde{\mathbf{x}}^i_{\mathrm{SM}}(t_n)$ at t_n. Here, $\tilde{\mathbf{x}}_{\mathrm{SM}}(t_n)$ represents the positions of all element vertices of the electromagnetic mesh which are contained in the sheet, $\mathbf{H}$ the shape function matrix evaluated at the local element coordinates ζ^i which corresponds to $\tilde{\mathbf{x}}^i_{\mathrm{SM}}(t_n)$. Next, all variable positions of $\tilde{\mathbf{x}}$ are adopted to $\tilde{\mathbf{x}}_{\mathrm{SM}}$ via the aforementioned smoothing technique yielding the new mesh topology of the

electromagnetic mesh at t_n. Figure 3 shows how the electromagnetic elements are moved according to the mechanically deformed mesh. Finally, the electromagnetic loads have to be mapped correctly onto the adapted mesh. As shown in Section 4, for typical frequencies and sheet thicknesses, the Lorentz force distribution in sheet thickness direction may vary in a highly non-linear way (see Figure 10). This motivates the separation of the algorithmic form of the weak momentum balance into a component that is purely mechanical and a component resulting from the electromagnetic loads,

$$\mathbf{f}_{n+1,n} = \mathbf{f}^{\mathrm{EM}}_{n+1,n}(\mathbf{x}_{n+1}, \mathbf{a}_{n+1}) + \mathbf{f}^{\mathrm{Mech}}_{n+1,n}(\mathbf{x}_{n+1}) \,. \tag{3}$$

Here, $\mathbf{f}^{\mathrm{EM}}_{n+1,n}$ represents the part attributed to the coupling by Lorentz forces. The structural force vector can be rewritten in terms of the usual assembly relation

$$\mathbf{f}_{n+1,n} = \sum\nolimits_e \mathbf{l}^{e\mathrm{T}}_{\mathbf{x}} (\mathbf{f}^{e\ \mathrm{EM}}_{n+1,n}(\mathbf{x}^e_{n+1}, \mathbf{a}^e_{n+1}) + \mathbf{f}^{e\ \mathrm{Mech}}_{n+1,n}(\mathbf{x}^e_{n+1})) \,. \tag{4}$$

Here, $\mathbf{f}^e_{n+1,n}$ represents the element contribution to the structural right hand side $\mathbf{f}_n$ which is assembled with the help of the element connectivity matrix $\mathbf{l}^e_{\mathbf{x}}$. More precise, the electromagnetic contribution $\mathbf{f}^{e\ \mathrm{EM}}_{n+1,n}$ is obtained via the usual integration over the element domain B^e_{r}

$$\mathbf{f}^{e\ \mathrm{EM}}_{n+1,n}(\mathbf{x}^e_{n+1}, \mathbf{a}_{n+1}) = -\int_{B^e_{\mathrm{r}}} \mathbf{H}^{\mathrm{T}} \det(\boldsymbol{F}^e(\mathbf{x}^e_{n+1}))\, \boldsymbol{\ell}^e_{n+1} \,. \tag{5}$$

It is important to note that the integration of (5) needs to be accurate in the direction where $\boldsymbol{\ell}^e_{n+1}$ decays (see Figure 10 and 7). Equation (5) is integrated via Gaussian quadrature [13]. The accurate rendering of the non-linear decay is archived by choosing a high number of Gaussian points in the thickness direction of the element domain of the solid shell element. Both, mapping of the deformation and transfer of the body forces are illustrated in Figure 3. The method proposed above was tested by means of a single mechanical element. To study

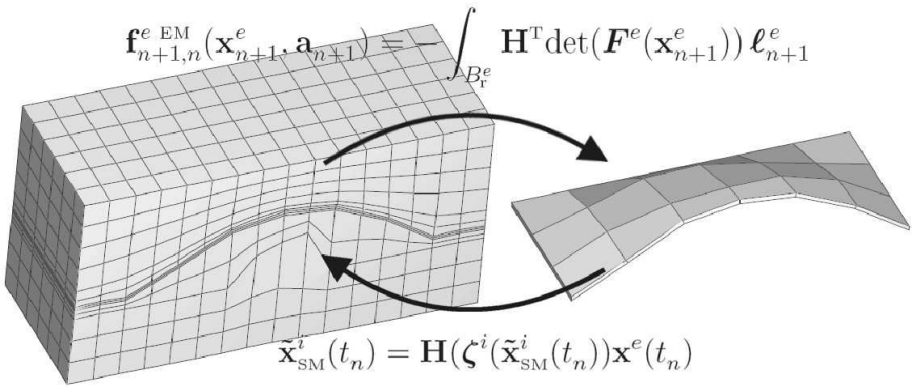

Figure 3: Data transfer in the context of the staggered solution algorithm at t_n. Body force data of the refined electromagnetic mesh are utilized to receive an accurate representation of the electromagnetic loading. The subsequent deformation of the sheet is mapped to its electromagnetic counterpart and the mesh the air is smoothly adapted.

the accuracy of $\mathbf{f}^{e\ \mathrm{EM}}_{n+1,n}$, the accuracy of both influencing factors, namely of the integration of

(5) and of ℓ^{e}_{n+1} at the integration points were investigated. For any fixed number of integration points the amount of electromagnetic elements contained in the mechanical element was increased and the corresponding sum of the vertical electromagnetic element loads was examined. Then, a current and a magnetic field distribution were imposed, both acting in the plane of the sheet metal and perpendicular to each other. Acording to the fully coupled case, both were chosen to decay exponentially. Figure 4 demonstrates the convergence of vertical loads when the number of electromagnetic elements and Gaussian points increase. Regardless of the number of Gaussian points, all curves start at the same value. If the shell contains just one electromagnetic element, the Lorentz force is assumed to be constant in the element and the nodal force result is independent of the accuracy of the integration. For the highest number of Gaussian points the nodal representation of the Lorentz force exhibits the best convergence. For lower numbers of Gaussian points the loads converge to values that are too small. A low number of Gaussian points implies that the bottom and top integration points are not located closely enough to the surface of the sheet, where body forces are maximal. This results in a pathological underestimation of the loads, which is also confirmed by an underestimation of the deformation of the sheet metal for the fully coupled simulation (see Figure 4). Since 8 Gaussian points ensure a sound integration with rather

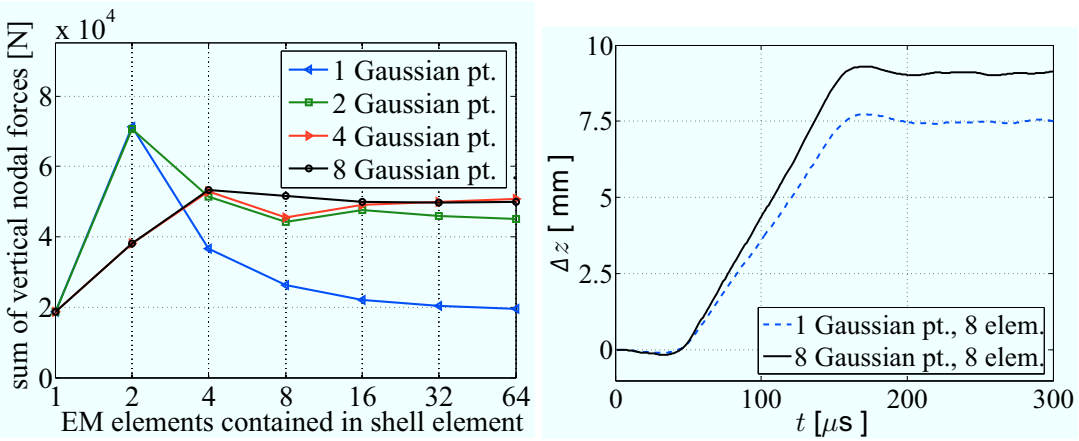

Figure 4: Accuracy of the mapping of body forces. Left: Convergence of the sum of vertical nodal forces with increasing number of elements and Gaussian points. Right: Influence of Gaussian quadrature on the vertical displacement at a specified point P2 close to the center of the plate determined by a fully coupled simulation. For a smaller number of Gaussian points electromagnetic loads are underestimated.

small additional numerical effort to integrate (5), we opt for this method, and all subsequent calculations were computed in this manner. Further, it can be seen that a good accuracy of the electromagnetic loads can be achieved by embedding at least 4 elements in the solid shell element.

3 Termination Criterion for the Electromagnetic Computation

As mentioned above, the largest computational effort is to be attributed to solving the electromagnetic part. It is important to note that external loading due to Lorentz forces typically takes place in the beginning of the process, during the first alternation of the tool coil current. Later, the amount of energy transferred to the sheet metal via electromagnetic loads is relatively small. At this time the actual forming takes place predominantly due to inertial forces. Hence a termination criterion that confidentially indicates the insignificance of the electromagnetic loads and thus enables to turn off the electromagnetic part allows for an enormous reduction in computational cost. In the field of non-linear finite element modeling convergence criteria commonly applied for the termination of global Newton Raphson schemes are usually based on the change of the energy of the corresponding Newton step in relation to the energy change of the first iteration

$$\Delta \mathbf{x}^{i}_{n+1,n} \cdot \mathbf{f}^{i}_{n+1,n} \leq \epsilon_c \Delta \mathbf{x}^{1}_{n+1,n} \cdot \mathbf{f}^{1}_{n+1,n} \, . \tag{6}$$

Here, $\Delta \mathbf{x}^{i}_{n+1,n} \cdot \mathbf{f}^{i}_{n+1,n}$ represents the energy change in terms of the deviation $\Delta \mathbf{x}^{i}_{n+1,n}$ of the nodal positions and the residual force vector $\mathbf{f}^{i}_{n+1,n}$ corresponding to the Newton step i. ϵ_c represents the tolerance for which (6) is fulfilled. Accordingly a termination criterion for the electromagnetic model is based on the energy transferred from the electromagnetic system to the mechanical one. If the amount of energy transferred after some time $t \geq t_{\text{ter}}$ is significantly smaller than the amount of energy that has been transferred up to this instance, it can be expected that an accurate representation of the mechanical deformation can be obtained without further consideration of the electromagnetic system. Therefore, with some tolerance ϵ_{EM} the electromagnetic simulation is stopped at termination time t_{ter} if

$$E_{\text{EM}}(\infty) - E_{\text{EM}}(t_{\text{ter}}) = \int_{t_{\text{ter}}}^{\infty} P_{\text{EM}} dt \leq \epsilon_{\text{EM}} \int_{0}^{t_{\text{ter}}} P_{\text{EM}} dt \tag{7}$$

is fulfilled. Here, $P_{\text{EM}}(t)$ represents the rate of energy transferred at instance t and $E_{\text{EM}}(t)$ the energy transferred from the electromagnetic system until instance t. Since the quantity $E_{\text{EM}}(\infty) - E_{\text{EM}}(t_{\text{ter}})$ is unknown, an alternative criterion based on the comparison of $P_{\text{EM}}(t)$ is employed. Here, the rate of energy at $t_{n+1,n}$ is estimated on the basis of the nodal velocities at t_{n+1} and the nodal representations of the electromagnetic loads given in (3)

$$P_{\text{EM}}(t_{n+1}) \approx \frac{(\mathbf{x}_{n+1} - \mathbf{x}_n) \cdot \mathbf{f}^{\text{EM}}_{n+1}}{t_{n+1,n}} \, . \tag{8}$$

In the particular case of EMF the rate of energy transferred to the mechanical part oscillates with decreasing amplitude as can be seen in Figure 5. This results from the oscillation of the input current. In particular during the first alternation, the largest amount of energy is transferred to the mechanical part. At later instances the intensity of the magnetic field is reduced due to the imposed input current and the expanded air gap between the sheet and the tool coil. Correspondingly, the peak values $P_{\text{EM}}(t_{Pi})$ of $P_{\text{EM}}(t)$ decay. In this case, relating the first peak value $P_{\text{EM}}(t_{P1})$ to the current peak value $P_{\text{EM}}(t_{Pi})$ represents a close match for the termination criterion given in (7) and represents a meaningful termination criterion. If the

energy contribution for $t \geq t_{Pi}$ is sufficiently small, the computation of the electromagnetic system can be terminated. In this respect the new termination criterion is denoted by

$$t_{ter} = t_{Pi} \text{ if } P_{\text{EM}}(t_{Pi}) \leq \epsilon_{\text{EM}} P_{\text{EM}}(t_{P1}) \, . \tag{9}$$

It is important to note that the value for ϵ_c in (6) can precisely be determined on the basis of the best possible numerical accuracy (usually $\epsilon_c = 1 \times 10^{-16}$). For ϵ_{EM} this is not the case. To show and quantify the effect of the termination of the electromagnetic simulation on the forming result, different values for ϵ_{EM} were chosen and the corresponding results were compared. Since the principal findings regarding the energy conversion are similar for coarse and fine meshes (see Section 4), a coarse mesh for the study of the termination criterion was chosen to save computation time.

Figure 5 shows the progression of P_{EM}. Each marker indicates the termination of the electromagnetic system corresponding to three different values for ϵ_{EM} attributed to 1.5%, 3% and 6% of the first peak value $P_{\text{EM}}(t_{P1})$. After terminating the electromagnetic simulation the total amount of energy $E_{\text{EM}}(t)$ transferred to the mechanical system remains constant which can be confirmed by the straight lines. The dotted red curve shows a simulation without termination of the electromagnetic system and serves as reference solution. Further, the graphs for the total amount of energy transferred $E_{\text{EM}}(t)$ indicate how the criteria are related to each other. As depicted in figures 5 and 6 the difference between the reference solution and the terminated one becomes smaller with decreasing ϵ_{EM} . Also interesting from the

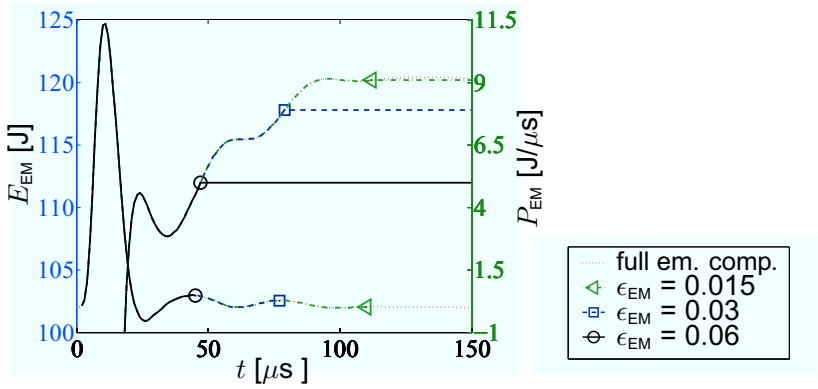

Figure 5: Termination criterion for different tolerances ϵ_{EM} corresponding to 1.5%, 3% and 6% of the first peak value $P_{\text{EM}}(t_{P1})$. To resolve the increase of E_{EM} due to subsequent alternations the left ordinate starts at 100 J. After termination of the electromagnetic part of the model P_{EM} = 0 and E_{EM} = const.

point of view of the technological process simulation is certainly the degree of deviation in terms of the deformation. To this end, the vertical displacement at a specified evaluation Point P2 close to the center of the plate was examined for the three values for ϵ_{EM}. As can be seen in the left part of Figure 6 only for ϵ_{EM} = 0.06 the deformation exhibits a significant underestimation (solid curve). For all other termination criteria the deformation is very close to the reference solution (dotted curve). To quantify this the displacement Δz and transferred energy E_{EM} at t = 300 μs were compared for the different termination criteria (see right part of Figure 6). Similar as in previous cases the relative deviation is highlighted by normalization

with the reference solution yielding the normalized values $\Delta\bar{z}$ and $\bar{E}_{\mathrm{EM}}$. Due to the nature of the termination criterion $\bar{E}_{\mathrm{EM}} < 1$. As a result of small elastic oscillations $\Delta\bar{z} > 1$ is possible for the comparison of the deformation. In view of subsequent simulations, ϵ_{EM} = 0.03 seems to represent a reasonable choice.

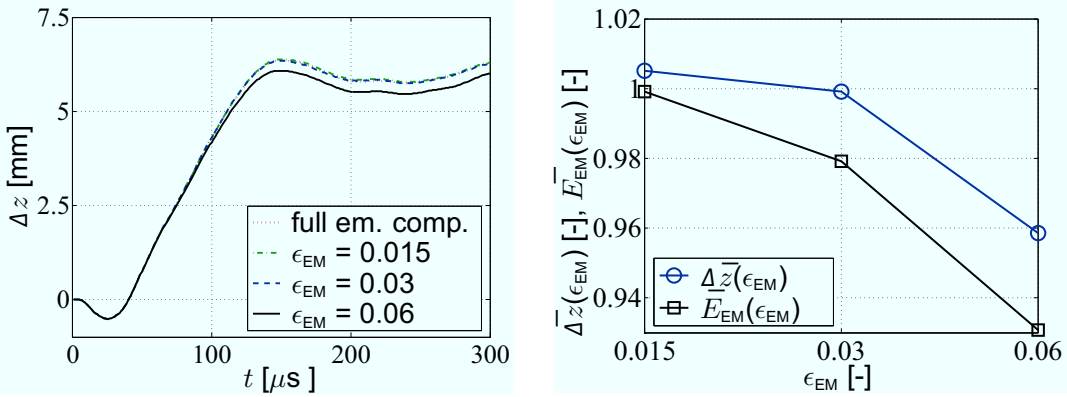

Figure 6: Influence of ϵ_{EM} on the vertical deformation at P2 and E_{EM}. Left: Vertical deformation with evolving time. Right: Normalized vertical deformation at t = 300 μs and E_{EM} depending on different values for ϵ_{EM}.

4 Discussion of Results for a Fully Coupled Simulation

With the above techniques at hand we now turn to the fully coupled simulation of the EMF process. As discussed above the energy driving the forming operation is characterized by the discharging current depicted in Figure 1 which was implemented as a Neumann boundary condition for χ. Starting from the right surface where χ = 0 is prescribed, the potential increases to a maximum value of χ = 4.1 kV to satisfy $(1)_3$ and the remaining Neumann boundary conditions. As could be expected, the *magnitude* of $\boldsymbol{j} = -\sigma_{\mathrm{EM}}\nabla_{\mathrm{s}}\chi$ inside the tool coil at t = 8 μs remains relatively unchanged, only $\boldsymbol{j}$ changes its direction following the centerline of the coil winding as can be seen in the center part of Figure 8. In the lower part of Figure 8, $\boldsymbol{j}$ is depicted for t = 40 μs. At this instance the input current has reached its second extreme value (see Figure 1) and flows in opposite direction. Accordingly the direction of $\boldsymbol{j}$ is flipped and has a reduced magnitude.

Next we turn to the development of the magnetic flux density $\boldsymbol{b}$ at the instances t = 4 μs, t = 12 μs and t = 28 μs. Up to t = 28 μs the largest portion of E_{EM} is transferred to the mechanical part of the model (see Figure 5). In this respect this period of time is significant for the forming operation. Due to the correlation of the tool coil current with the input current, also $\boldsymbol{b}$ is correlated to the input current via Ampere's law. As can be seen by comparison of Figure 7 (above) and Figure 7 (center) the increased input current at t = 12 μs results in an increase of $\boldsymbol{b}$. At t = 28 μs where I just flipped (see Figure 7 (below)) the current in the tool coil and so $\boldsymbol{b}$ are small. At all instances $\boldsymbol{b}$ is insignificant above the sheet metal. This can be attributed to the eddy currents induced in the sheet metal (see Figure 7). Here, the temporal evolution of the magnetic field becomes important. The increase

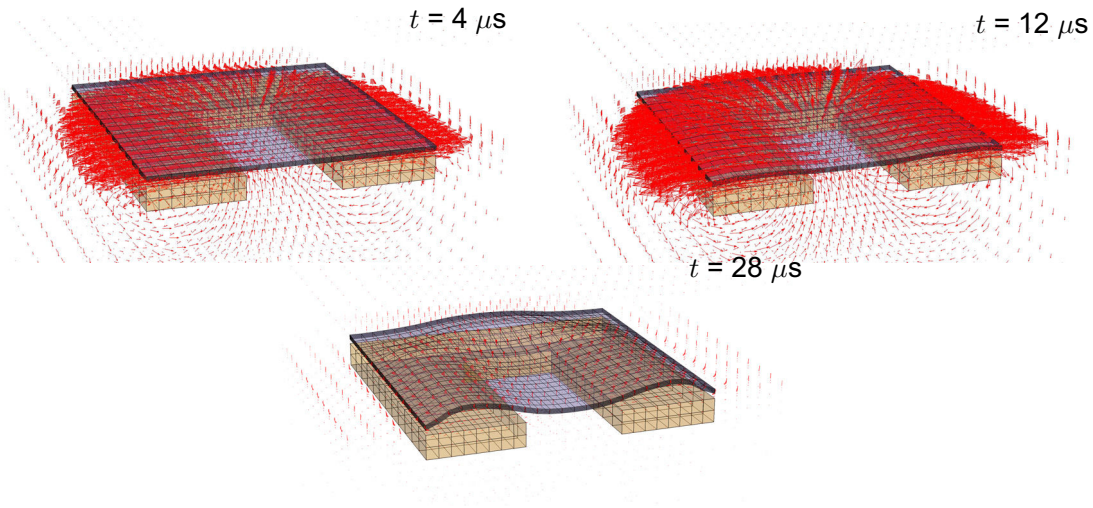

Figure 7: Magnetic flux density distribution for the instances t = 4 μs, t = 12 μs and t = 28 μs. With increasing input current I the magnetic flux density $\boldsymbol{b}$ increases as well. The shielding effect of the sheet metal becomes evident.

of I until t = 8 μs leads to an increase of $\boldsymbol{b}$ in the air in the center of the tool coil winding. The magnetic field and its increase $\partial\boldsymbol{b}$ are oriented in z-direction here. According to Faraday's law of induction, $\partial\boldsymbol{b}$ induces an electric field which drives eddy currents which proceed along the tool coil winding and are oriented in opposition to the current in the winding. Due to their orientation, these eddy currents neutralize the magnetic field above and inside the sheet metal and lead to the shielding effect. Furthermore at t = 12 μs in contrast to t = 4 μs, $\boldsymbol{b}$ begins to penetrate the sheet metal which can be seen by the vectors of $\boldsymbol{b}$ at the upper surface of the sheet metal. This is discussed below together with the development of the eddy currents in the sheet metal.

In Figure 7 the eddy current distributions for the aforementioned instances are shown. In more detail this is depicted in Figure 10 where the significant components j_y of $\boldsymbol{j}$ and b_x of $\boldsymbol{b}$ are depicted along PZ with increasing time. Since the sheet metal deforms under the influence of the Lorentz force the current flux distributions move in vertical direction with increasing time. At the beginning of the process, where the input current exhibits a significant increase, the magnetic field increases in particular close to the lower surface of the sheet metal while an increase inside the sheet metal is relatively small. Accordingly eddy currents occur close to the lower surface as well (see instance t = 4 μs Figure 10) to counter the local penetration of $\boldsymbol{b}$. Later, when the first alternation reached its peak at t = 8 μs as discussed above, $\boldsymbol{b}$ becomes maximal and remains constant outside the sheet metal and the increase close to the surface of the sheet metal is reduced. Accordingly the eddy currents induced here are reduced in comparison to t = 4 μs. *Inside* the sheet metal, however, $\partial\boldsymbol{b}$ might be larger than at previous instances due to the fact that further penetration of $\boldsymbol{b}$ in the sheet metal is facilitated. This in turn leads to an induction of eddy currents into regions which are more distant from the lower surface. As can be seen in Figure 10 at t = 4 μs the eddy currents close to the upper surface are insignificant and so is the magnetic flux density. While proceeding further to t = 8 μs inside the sheet metal, b_x has risen, consequently even close

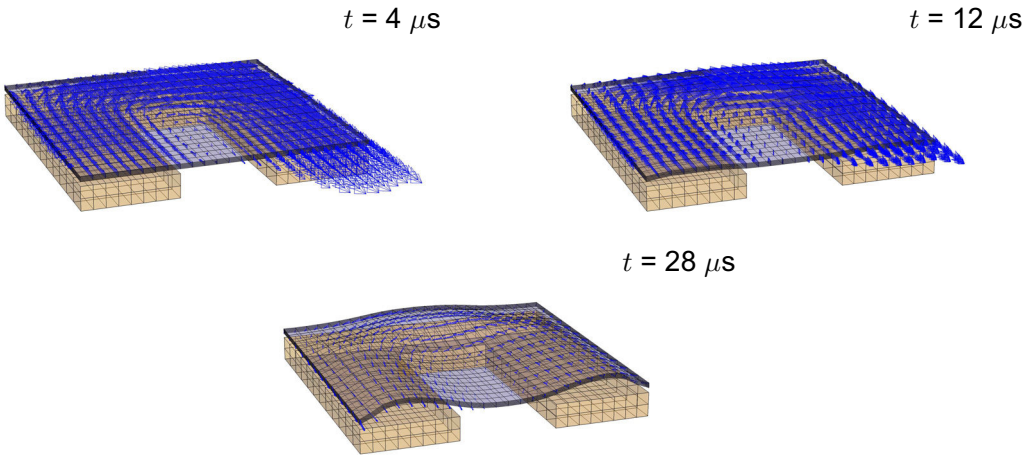

Figure 8: Eddy current distribution for the instances t = 4 μs, t = 12 μs and t = 28 μs. At the beginning of the process the increase of $\boldsymbol{b}$ in the air results in high values for the induced eddy currents at the surface of the sheet metal. At later instances $\boldsymbol{b}$ increases inside the sheet and leads to a more homogenous eddy current distribution in thickness direction.

to the upper surface j_y has become significant while close to the lower surface j_y is reduced. With increasing time (see, *e.g.*, t = 12 μs) the magnetic field in the air gap decreases, then the eddy currents close to the surface become smaller than inside the sheet metal where the penetration of the magnetic field still leads to an increase of b_x. Close to the lower surface now the effect of self induction of the sheet leads to a retention of the eddy currents although $\boldsymbol{b}$ decreases in the air gap. At t = 20 μs and later instances, the eddy current direction is even reversed close to the lower surface of the sheet metal. The flipped eddy currents at the surface of the sheet superimpose a magnetic field to that of the tool coil which leads to a further reduction of the magnetic flux density at the surface of the sheet. The maximal value for b_x is now inside the sheet (see Figure 10 instances t = 20 μs, t = 24 μs and t = 28 μs) and the maximal value for j_y at its upper surface.

Referring to the Lorentz force $\boldsymbol{l}_r$ = det($\boldsymbol{F}$)$\boldsymbol{j} \times \boldsymbol{b}$ as a coupling term to the mechanical component the above discussion underlines the fact that special care has to be taken to account for the strong variations of $\boldsymbol{b}$ and $\boldsymbol{j}$ in the sheet metal (see Section 2). Further it could be seen that $\boldsymbol{b}$ and $\boldsymbol{j}$ penetrate the sheet metal at instances where they are still significant in terms of their magnitude (see *e.g.*, t = 8 μs in Figure 10), in this respect the notion of a magnetic pressure [14] in the context of EMF is not accurate since $\boldsymbol{b}$ and $\boldsymbol{j}$ and so the Lorentz force act inside the sheet metal. Regarding the development of $\boldsymbol{b}$ and $\boldsymbol{j}$ with respect to the progression of the forming operation from figure 7 it can be seen that $\boldsymbol{l}_r$ predominantly acts in positive vertical direction and evolves below the tool coil winding. This applies to all alternations regardless of the direction of the input current, $\boldsymbol{b}$ and $\boldsymbol{j}$ basically flip simultaneously. Only at some time shortly before zero-crossing of the input current $\boldsymbol{b}$ and $\boldsymbol{j}$ are oriented such that $\boldsymbol{l}_r$ points downwards (see Figure 10, instances t = 20 μs and t = 24 μs).

The temporal development of $\boldsymbol{l}_r$ can be deduced from Figure 10. While at the very

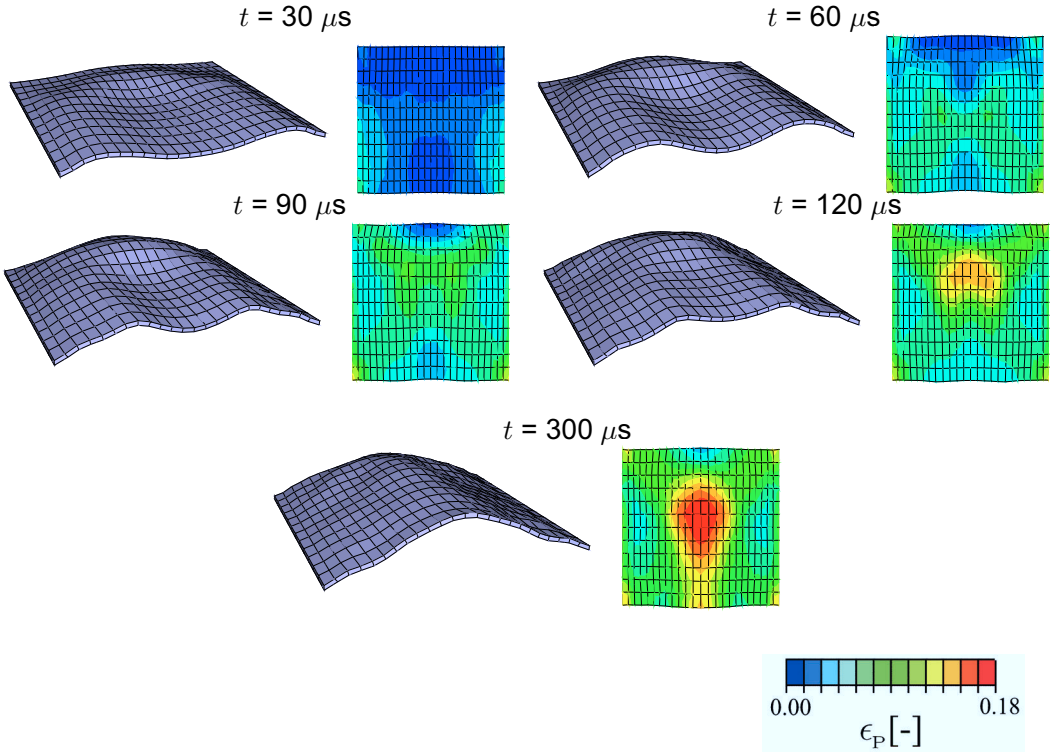

Figure 9: Forming stages of the sheet metal as a function of time and corresponding top view contour plots of ϵ_P. Initially, the part of the sheet metal lying directly over the tool coil is subject to large induced Lorentz forces and begins to accelerate. As forming proceeds, this part pulls the center of the plate along with it.

beginning of the process the largest eddy currents are induced, the magnetic flux density is still relatively small since the tool coil current is relatively small as well; moreover the sheet metal is basically at rest meaning that very little energy is transferred to the mechanical system. At some time between t = 4 μs and t = 20 μs where both, the velocity of the sheet metal and $\boldsymbol{l}_r$ = det($\boldsymbol{F}$) $\boldsymbol{j} \times \boldsymbol{b}$ are relatively large, the forming operation is most effective. In fact this motivates the redesign of the electric circuit attached to the forming setup – presently basically consisting of a switch and a capacitor – such that the efficiency of the process can be increased.

The aforementioned Lorentz force distribution is also reflected by the stages of deformation depicted in Figure 9. At the beginning of the process, the center of the plate remains at rest, whereas just above the tool coil winding, the plate experiences high Lorentz forces and begins to accelerate (see Figure 9, instance t = 30 μs). The contour plots represent the development of the accumulated inelastic deformation for this stage of deformation as a top view of the sheet metal. Due to the boundary conditions of the sheet metal for t = 30 μs the lateral regions exhibit an increase of ϵ_P, the rear part of the structure exhibits no inelastic deformation due to the fact that the sheet metal can move freely and $\boldsymbol{l}_r$ is less pronounced here The lateral fixing leads to a combined bending and stretching of the sheet caused by the body force distribution nearby. In particular at the front corners of the sheet the inelastic deformation exhibits its maximal value of $\epsilon_P \approx 0.8$. The loading of the plate leads to a lateral

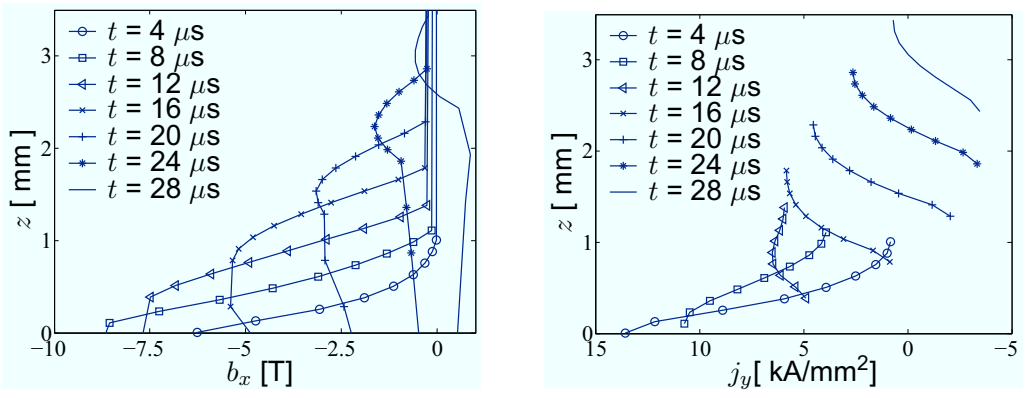

Figure 10: Development of b_x and j_y along PZ with evolving time and deformation. Left: The development of b_x in the sheet and surrounding air. Right: Development of eddy currents in the sheet. Curves for j_y move according to the vertical deformation of the sheet.

contraction of the plate which becomes zero at the fixed edge of the plate. The strains resulting from this lateral deformation, however, are maximal here and contribute to the increase of ϵ_P. With increasing time (see Figure 9, t = 60 μs) the accelerated parts of the structure continue to deform and the center of the plate – initially at rest – begins to move. In addition to the front corners of the sheet metal now the rear corners exhibit an increased inelastic deformation as well and bands of increased inelastic deformation propagate from the front corners to the center of the sheet. At t = 90 μs and t = 120 μs the center of the plate is accelerated further, the bands of deformation evolve and close to the center of the plate a maximum for ϵ_P starts to develop. The final shape of the structure for t = 300 μs is shown in the last image of Figure 9. During the last forming stages the initially downwards bent center of the structure is now pulled along with the lateral regions of the plate and bent upwards resulting in a roof-top shaped structure. The strong inelastic bending results in an additional increase of ϵ_P at the center of the plate.

References

[1] *Takatsu, N.*; *Kato, M.*; *Sato, K.*; and *Tobe, T.*: High-speed forming of metal sheets by electromagnetic forces. International Journal of the Japanese Society for Mechanical Engineering, volume 31: pp. 142–148, 1988.

[2] *Gourdin, W. H.*; *Weinland, S. L.*; and *Boling, R. M.*: Development of the electromagnetically-launched expanding ring as a high strain-rate test. Review of Scientific Instruments, volume 60: pp. 427–432, 1989.

[3] *Fenton, G.* and *Daehn, G. S.*: Modeling of electromagnetically formed sheet metal. Journal for Materials Processing Technology , volume 75: pp. 6–16, 1998.

[4] *Oliveira, D.*; *Worswick, M.*; and *Finn, M.*: Finite Element Modelling of the Electromagnetic Forming of Aluminum Alloy Sheet. In *Proceedins of 4th International ESAFORM Conference on Material Forming*, pp. pp. 773–776. Liége, Belgium, 2001.

[5] *Imbert, J.*; *Winkler, S.*; *Worswick, M.*; *Oliveira, D.*; and *Golovashchenko, S.*: Numerical Modeling of an Electromagnetic Corner Fill Operation. In *Proceedings of NUMIFORM 2004*, pp. pp. 1833–1839. Ohio State University, USA, 2004.

[6] *Schinnerl, M.*; *Schöberl, J.*; *Kaltenbacher, M.*; and *Lerch, R.*: Multigrid methods for the 3D simulation of nonlinear magneto-mechanical systems. IEEE Transactions on Magnetics, volume 38(3): pp. 1497–1511, 2002.

[7] *Svendsen, B.* and *Chanda, T.*: Continuum thermodynamic formulation of models for electromagnetic thermoinlastic materials with application to electromagnetic metal forming. Cont. Mech. Thermodyn., volume 17: pp. 1–16, 2005.

[8] *Stiemer, M.*; *Unger, J.*; *Blum, H.*; and *Svendsen, B.*: Algorithmic formulation and numerical implementation of coupled electromagnetic-inelastic continuum models for electromagnetic metal forming. Int. J. Numer. Methods Engrg., volume 68: pp. 1301–1328, 2006.

[9] *Stiemer, M.*; *Unger, J.*; *Blum, H.*; and *Svendsen, B.*: Algorithmic formulation and numerical implementation of coupled electromagnetic-inelastic continuum models for electromagnetic metal forming. In *Proceedings of ECCOMAS CFD European Conference on Computational Fluid Dynamics*, pp. pp. 362–382. Egmond aan Zee, The Netherlands, 2006.

[10] *Reese, S.*: A large deformation solid-shell concept based on reduced integration with hourglass stabilization. International Journal for Numerical Methods in Engineering, volume 69: pp. 1671–1716, 2007.

[11] *Jackson, J. D.*: *Classical Electrodynamics*. John Wiley and Sons, 1975.

[12] *Field, D.*: Laplacian smoothing and Delaunay triangulations. Communications in applied numerical methods, volume 4: pp. 709–712, 1988.

[13] *Hughes, T. J. R.*: *The Finite Element Method*. Prentice-Hall, 1987.

[14] *Mamalis, A.*; *Manolakos, D.*; *Kladas, A.*; and *Koumoutsos, A.*: Electromagnetic forming and powder processing: Trends and developments. Appl. Mech. Rev., volume 57(4): pp. 299–324, 2004.